Hyoungsoon Lee[1,2]
Mechanical Engineering Department,
Stanford University,
Stanford, CA 94305
e-mail: lee8191@stanford.edu

Damena D. Agonafer[2]
Mechanical Engineering Department,
Stanford University,
Stanford, CA 94305

Yoonjin Won
Mechanical and Aerospace Engineering,
University of California at Irvine,
Irvine, CA 92697

Farzad Houshmand
Mechanical Engineering Department,
Stanford University,
Stanford, CA 94305

Catherine Gorle
Department of Civil Engineering and
Engineering Mechanics,
Columbia University,
New York, NY 10027

Mehdi Asheghi
Mechanical Engineering Department,
Stanford University,
Stanford, CA 94305

Kenneth E. Goodson
Mechanical Engineering Department,
Stanford University,
Stanford, CA 94305

Thermal Modeling of Extreme Heat Flux Microchannel Coolers for GaN-on-SiC Semiconductor Devices

Gallium nitride (GaN) high-electron-mobility transistors (HEMTs) dissipate high power densities which generate hotspots and cause thermomechanical problems. Here, we propose and simulate GaN-based HEMT technologies that can remove power densities exceeding 30 kW/cm^2 at relatively low mass flow rate and pressure drop. Thermal performance of the microcooler module is investigated by modeling both single- and two-phase flow conditions. A reduced-order modeling approach, based on an extensive literature review, is used to predict the appropriate range of heat transfer coefficients associated with the flow regimes for the flow conditions. Finite element simulations are performed to investigate the temperature distribution from GaN to parallel microchannels of the microcooler. Single- and two-phase conjugate computational fluid dynamics (CFD) simulations provide a lower bound of the total flow resistance in the microcooler as well as overall thermal resistance from GaN HEMT to working fluid. A parametric study is performed to optimize the thermal performance of the microcooler. The modeling results provide detailed flow conditions for the microcooler in order to investigate the required range of heat transfer coefficients for removal of heat fluxes up to 30 kW/cm^2 and a junction temperature maintained below 250 °C. The detailed modeling results include local temperature and velocity fields in the microcooler module, which can help in identifying the approximate locations of the maximum velocity and recirculation regions that are susceptible to dryout conditions. [DOI: 10.1115/1.4032655]

Keywords: microchannel heat sinks, multiscale modeling, GaN-on-SiC

1 Introduction

Gallium nitride (GaN) HEMTs have received considerable attention over the last decade due to the material characteristics that improve electrical performance [1]. Thermal management of high radio frequency power devices using GaN HEMT has become an important issue since the maximum power output of the GaN HEMT is often thermally limited, which leads to significant degradation of amplifier performance and system reliability [2–4].

Silicon carbide (SiC) substrates are commonly adopted for thermal management of GaN HEMT devices due to its performance and thermal conductivity (370 W/m K). However, it is crucial to maintain a low operating temperature since the thermal conductivity of SiC decreases as temperature increases [5]. Direct liquid cooling with microchannel heat sinks using high thermal conductivity material at the impingement surface is a viable and preferred option for thermal management of GaN-on-SiC electronics. Innovations in microfluidic geometries including hierarchical nanostructures and three-dimensional (3D) manifold designs bring significant enhancement of cooling performances [6]. Calame et al. [7] developed direct-die-attached microchannel heat sinks using a wide variety of materials for thermal management of GaN-on-SiC semiconductor devices and demonstrated a maximum heat flux of 1.5 kW/cm^2 on a SiC chip of 3×5 mm^2 heated area. Escher et al. [8] proposed an ultrathin manifold microchannel heat sink using silicon-based microfabrication and achieved cooling power densities of more than 700 W/cm^2. Cetegen [9] proposed and tested a novel 3D manifold design with force-fed grooved microchannels that consisted of thin copper layers. They achieved heat fluxes up to 1.23 kW/cm^2 using R245fa while maintaining a significantly lower thermal resistance and pressure drop compared to conventional two-dimensional microchannel heat sinks. Recent developments in microfabrication allow microchannels to be integrated directly onto the substrates which eliminates the need for thermal interfacial materials, can lead to a decrease in the overall thermal resistance [10].

There have been studies which demonstrated a fabrication method for a five-layer stacked die with die-embedded high aspect ratio microchannels using through-silicon-vias; however, only the hydrodynamic performance of the manifold was considered [11]. Everhart et al. [12] fabricated and tested a microcooler on a 1 mm-thick silicon wafer using deep reactive ion etching to create both $20\,\mu\text{m} \times 200\,\mu\text{m}$ microchannels and manifold channels and bonded the SiC diode using a gold tin eutectic bond. Their experimental results show excellent thermal performance with maximum heat fluxes over 600 W/cm^2.

[1]Corresponding author.
[2]H. Lee and D. D. Agonafer contributed equally to this work.

Contributed by the Electronic and Photonic Packaging Division of ASME for publication in the JOURNAL OF ELECTRONIC PACKAGING. Manuscript received October 1, 2015; final manuscript received December 28, 2015; published online March 10, 2016. Assoc. Editor: Toru Ikeda.

Here, we examine the cooling limits of a microcooler module that can dissipate heat fluxes exceeding 30 kW/cm^2 at the device footprint. The current microcooler design includes multiple microchannels directly fabricated on a SiC substrate to minimize the thermal resistance from the hotspot to coolant [13]. A U-bend shaped 3D manifold inlet/outlet is adopted for a path for coolant to flow in order to enhance the heat transfer coefficient at the walls of the microchannel while maintaining a low pumping power. To investigate the thermofluid design of the microcooler, two modeling approaches are employed in this work: (1) a conduction model and (2) a single- and two-phase conjugate heat transfer model. A single- and two-phase conjugate simulation heat transfer model for a single channel using ANSYS FLUENT provides insight on the detailed flow pattern, local heat transfer coefficients, and pressure drops in various segments of the flow channel. However, it is impractical to investigate all the possible operating conditions since both single- and two-phase conjugate simulations are computationally expensive compared to a conduction simulation. Therefore, we first develop a solid conduction model for the entire microcooler structure using COMSOL MULTIPHYSICS to explore temperature distributions of the microcooler in different heat transfer coefficients. Then, both single- and two-phase conjugate simulations are developed only for selected operating conditions which are obtained from the solid conduction simulation results, which meet the design criteria. Our results provide preliminary supportive evidence for using embedded SiC microchannels with a 3D manifold for cooling of high power density electronics.

2 Flow Boiling Heat Transfer and Flow Regimes

2.1 Geometry Description of Microcooler. Figure 1 shows a schematic of the proposed microcooler design. The microcooler device has GaN and SiC substrates on 1700 μm $\times$ 600 μm area. The GaN has 40 multiple channels of 2 μm $\times$ 350 μm that dissipate up to 330 kW/cm^2. A 1.5 μm-thick GaN layer is located underneath the gates, and a 10 μm-thick SiC layer is attached to improve heat spreading from the gate to the SiC substrate. Eighty-five microchannels are directly fabricated into the SiC substrate and each channel has a 9:1 aspect ratio (10 μm width $\times$ 90 μm height), which is feasible using an inductive coupled plasma etching technique [13]. Methanol is used as the working fluid due to its superior thermal conductivity and latent heat of evaporation. The working fluid enters at the center of the microchannel to exploit impingement cooling and to minimize the flow path. After flowing through a 200 μm length microchannel, the fluid exits from the channel ends. Details are provided in Sec. 4.

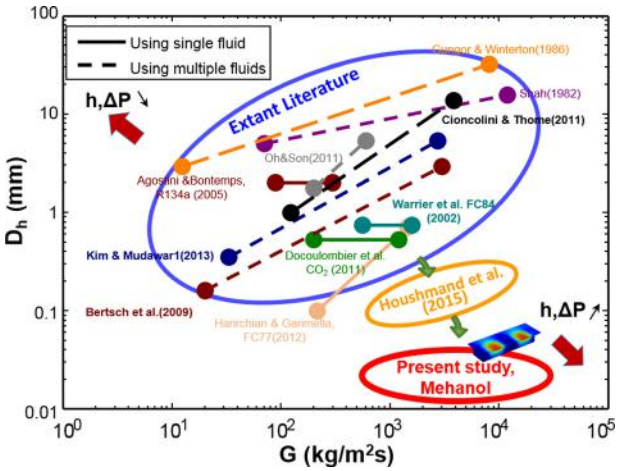

Fig. 2 Hydraulic diameter and mass velocity ranges for various correlations

2.2 Relevant Flow Boiling Heat Transfer Correlations. There are numerous predictive flow boiling heat transfer correlations available in the literature [14]. However, it is important to investigate the valid application ranges of these correlations since the heat transfer mechanism is dependent on several parameters including the geometrical configuration, flow regime, and working fluid used for the system. Figure 2 is the existing heat transfer correlations map that summarizes the ranges of hydraulic diameters and mass fluxes found in the literature and is plotted with the current microcooler design conditions. The solid lines are for correlations developed based on the experimental data using a single type of working fluid, while the dashed lines are for correlations developed based on a consolidated database using more than two different working fluids. It should be noted that none of the aforementioned correlations were developed based on mass flux and hydraulic diameter to the present microcooler design. For example, the hydraulic diameter of the present microcooler device is more than two orders of magnitude smaller compared to correlations found in the literature with similar ranges of mass flux.

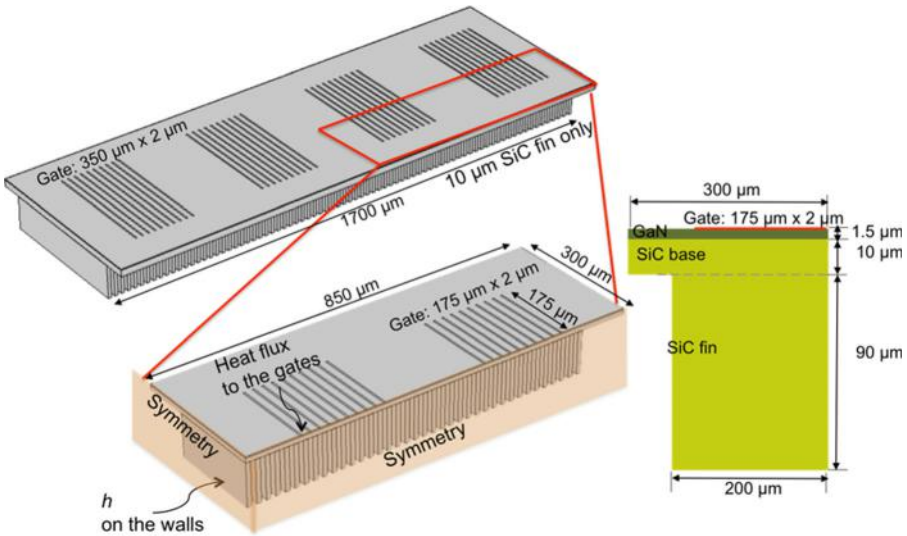

Fig. 1 Three-dimensional view of (*a*) the system level device, (*b*) quarter-symmetry device, and (*c*) cross-sectional view of the microchannel, which shows a 1.5 μm-thick GaN layer, 10 μm-thick SiC base, and 90 μm-thick SiC fin

2.3 Investigation of Flow Regimes for Present Study. We here study the flow regime using two existing correlations that used similar hydraulic ranges to the present microcooler design. The Costa-Patry and Thome [15] developed a flow regime correlation based on the operating conditions of $G = 100$–$1100\,\text{kg/m}^2$ s and $q'' = 0.8$–$26\,\text{kW/cm}^2$ for a hydraulic diameter range of $D_h = 0.146$–$3.04\,\text{mm}$. It predicts the transition to annular flow for the present design occurs at a relatively low vapor quality of $x = 0.057$–0.012 for $G = 6000$–$24{,}000\,\text{kg/m}^2$ s

$$x_{\text{CB-AF}} = 425\left(\frac{\rho_g}{\rho_f}\right)^{0.1}\frac{\text{Bo}^{1.1}}{\text{Co}^{0.5}} \tag{1}$$

where Bo and Co are the boiling number ($\text{Bo} = q''/(Gh_{fg})$) and the confinement number ($\text{Co} = \sqrt{\sigma/g(\rho_f - \rho_g)}/D_h$), respectively. Figure 3 shows the flow regime map comparison of the present operating conditions using Lee et al. [16]. These authors send the modified Weber number, We*, and the Lockhart–Martinelli parameter, X_{tt}, to construct a balance between the destructive and stabilizing forces acting on the liquid film, which are expressed as

$$\text{We}^* = 2.45\,\text{Re}_g^{0.64}\left(\frac{\mu_g^2}{\rho_g\,\sigma\,D_h}\right)^{0.3}\Big/\varphi_g^{0.4}\quad\text{for Re}_f \le 1250 \tag{2a}$$

and

$$\text{We}^* = 0.85\,\text{Re}_g^{0.79}\left(\frac{\mu_g^2}{\rho_g\,\sigma\,D_h}\right)^{0.3}\left[\left(\frac{\mu_g}{\mu_f}\right)^2\left(\frac{\rho_f}{\rho_g}\right)\right]^{0.084} \times\left(\frac{X_{tt}}{\varphi_g^{2.55}}\right)^{0.157}\quad\text{for Re}_f > 1250 \tag{2b}$$

where

$$\text{Re}_g = x\,G\,D_h/\mu_g \tag{3a}$$

$$\text{Re}_f = G\,(1-x)\,D_h/\mu_f \tag{3b}$$

$$X_{tt} = \left(\frac{1-x}{x}\right)^{0.9}\left(\frac{\rho_g}{\rho_f}\right)^{0.5}\left(\frac{\mu_f}{\mu_g}\right)^{0.1} \tag{3c}$$

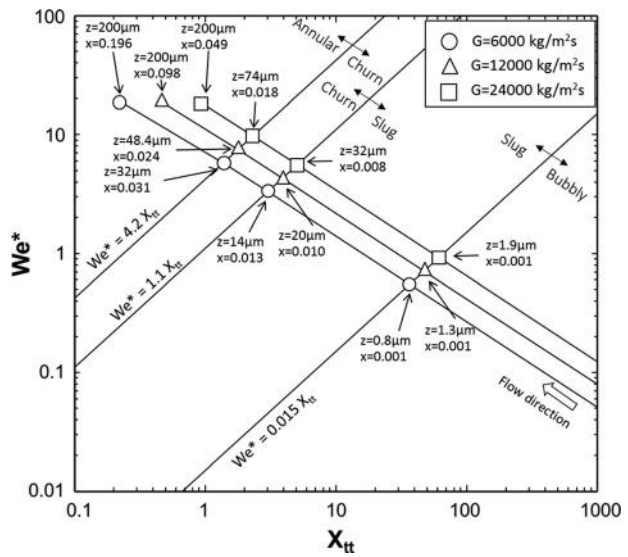

Fig. 3 Flow regime data compared to regime map proposed by Lee et al. [16]

and

$$\phi_g = 1 + 1.09\,X_{tt}^{0.039} \tag{3d}$$

As shown in Fig. 3, the major portion of the channel for all the three mass velocities of $G = 6000$, 12,000, and $24{,}000\,\text{kg/m}^2$ s is within the annular flow regime. However, a quarter of the channel contains different flow regimes including bubbly, slug, and churn.

3 Conduction Simulation

3.1 Geometry Description for Conduction Simulation. A conduction simulation is performed using COMSOL MULTIPHYSICS to account for the thermal resistances associated with the GaN, SiC substrates, and SiC channels for the microcooler as shown in Fig. 1. COMSOL MULTIPHYSICS is used to examine each thermal resistance and temperature rise between the junction and the fin walls by solving for the temperature field as the solution to the steady-state heat conduction equation below:

$$-n\cdot(-k\nabla T) = q'' \tag{4}$$

where k is the thermal conductivity of each layer and T is the temperature.

3.2 Boundary Conditions. A total power of 92.4 W is applied to the gates resulting in a heat flux of $330\,\text{kW/cm}^2$ in the $2\,\mu\text{m} \times 175\,\mu\text{m}$ gates region and $30\,\text{kW/cm}^2$ to $350\,\mu\text{m} \times 220\,\mu\text{m}$ in the active area. A range of heat transfer coefficients is imposed to the fin walls as an independent variable in order to investigate its impact on the maximum junction temperature. The range of heat transfer coefficients is selected based on the relevant two-phase correlations as well as single-phase simulation results (see Sec. 3.3). Quarter-symmetry is assumed and as such boundary conditions are assigned to two surfaces of device as shown in Fig. 1(*b*). The remaining surfaces are considered adiabatic. The models account for the thermal conductivity of GaN and SiC as a function of temperature as indicated in Table 1.

3.3 Relevant Correlations. As discussed earlier, there are no available correlations to predict the present geometry. We therefore select four different two-phase boiling correlations that have operating conditions near our design conditions. A flow boiling experiment is separately conducted using microtubes for a hydraulic diameter range of $D_h = 150$–$265\,\mu\text{m}$ with mass velocities up to $G = 10{,}000\,\text{kg/m}^2$ s in order to examine the aforementioned correlations for the current design [17]. Kim and Mudawar [18] and Bertsch et al. [19] developed universal correlations based on a consolidated database with wide ranges of mass flux, hydraulic diameter, flow regimes, and heat flux. The Cioncolini and Thome [20] correlation is used to calculate the heat transfer coefficient specifically for an annular flow dominant regime due to the early

Table 1 Thermodynamic properties used in the study

	Methanol	
	Liquid	Vapor
ρ	$742.8\,\text{kg/m}^3$	$1.5\,\text{kg/m}^3$
C_p	2520 J/kg K	4536 J/kg K
k	0.2011 W/m K	0.0209 W/m K
μ	$30.62 \times 10^{-5}\,\text{kg/m s}$	$1.1 \times 10^{-5}\,\text{kg/m s}$
h_{fg}	1090.1 kJ/kg	
	SiC	
k	$0.0038\,T^2 - 4.1734\,T + 1259$ W/m K, T (in K), <600 K	
	GaN	
k	$-0.1623\,T + 214.17$ W/m K, T (in K)	

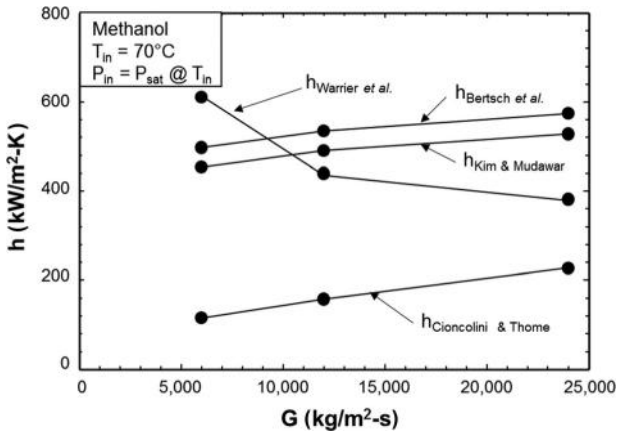

Fig. 4 Heat transfer coefficients for three different mass fluxes of $G = 6000$, 12,000, and 24,000 kg/m^2 s obtained from four different correlations

transition as indicated in Sec. 2.3. Warrier et al. [21] correlation is also utilized to predict a heat transfer coefficient for nucleate boiling dominant regimes as (e.g., bubbly flow) shown in Fig. 3.

Figure 4 shows the range of heat transfer coefficient values obtained from selected correlations for three different mass fluxes of $G = 6000$, 12,000, and 24,000 kg/m^2 s. Warrier et al. [21] correlation predicts the highest heat transfer coefficient at the lowest mass flux of $G = 6000$ kg/m^2 s and decreases due to nucleate boiling suppression as G increases. The Cioncolini and Thome [20] correlation underpredicts the heat transfer coefficients compared to those from other correlations since it is only based on the convective boiling dominant experimental data. Overall, calculated heat transfer coefficients have a range of $h = 116$–605 kW/m^2 K for mass velocities of $G = 6000$–24,000 kg/m^2 s for the present microcooler channel configuration.

3.4 Conduction Simulation Results and Discussion. Conduction simulation results with a constant heat transfer coefficient at the microchannel walls are shown in Fig. 5. Here, we set a heat transfer coefficient of 400 kW/m^2 K, which is the median value from the relevant correlation study. The figure indicates the temperature distribution of the quarter-symmetry device, top surface, and fin surface. For the details of temperature distribution, the temperature profiles along the x-direction at the top surface and the z-direction below the hotspot are plotted in Fig. 6. Figure 6(*a*) shows the temperature profile associated with gate locations and indicates a significant temperature difference of ~80 °C between the center gate and end gate. The large temperature variation between gate locations may introduce flow instability. The temperature rise in Fig. 6(*b*) shows the contribution of each layer to the total thermal resistance from the junction to the working fluid. The results of using an h of 400 kW/m^2 K show a ΔT of 20 °C, 45 °C, and 100 °C from the GaN layer, SiC base, and SiC fins, respectively. Thus, the dominant temperature rise is from SiC fins, and a more efficient operating condition associated with higher heat transfer coefficients should be considered to decrease the thermal resistance of SiC fins and to minimize the junction temperature (see Ref. [13] for more details on temperature changes in different heat transfer coefficients and channel geometries).

The maximum junction temperature and maximum wall temperature at the fin base are plotted as increasing heat transfer coefficients in Fig. 7. The solid red line indicates the junction temperature from the solid simulation models. We compare the results to the relevant heat transfer correlations (□) and single-phase conjugate CFD models (Δ). The performance of the GaN HEMT devices degrades at higher junction temperatures due to the temperature-dependent thermal conductivity of GaN and SiC. Therefore, one of the challenges for thermal management is to maintain the junction temperature below a target of 250 °C. The conduction simulation models estimate the junction temperature from 250 to 350 °C with varying h from 200 to 600 kW/m^2 K. Higher heat transfer coefficients associated with higher mass fluxes decrease the junction temperatures while simultaneously increasing the pressure drop. The simulation models estimate the maximum wall temperature as indicated with a black solid line in Fig. 7, while the maximum wall temperature decides the quality level of working fluid and resulting thermofluidic performance of the microcooler (i.e., pressure drop and coefficient of performance (COP)). For example, the models predict the maximum wall temperature from 200 to 300 °C with varying h of 200–600 kW/m^2 K. While the suggested working fluid, methanol, has a saturation temperature of 70 °C, the two-phase model should be considered to provide insights into the thermal performance associates with the flow regimes.

4 Conjugate CFD Simulation

The single-phase and two-phase CFD simulations are performed for a single microchannel to investigate flow patterns, local heat transfer coefficients, and pressure drops in various

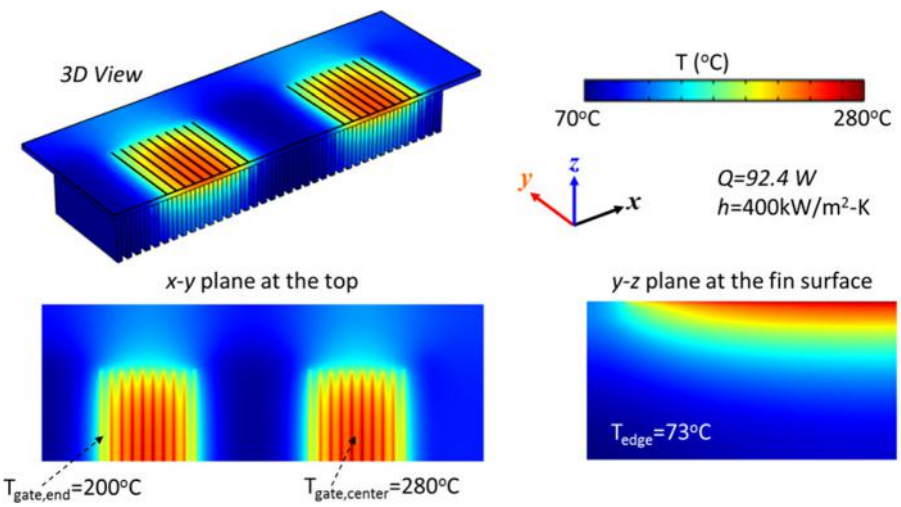

Fig. 5 Temperature distributions of the quarter-symmetry device, top surface, and fin side surface when an h of 400 kW/m^2 K is imposed on the fin walls

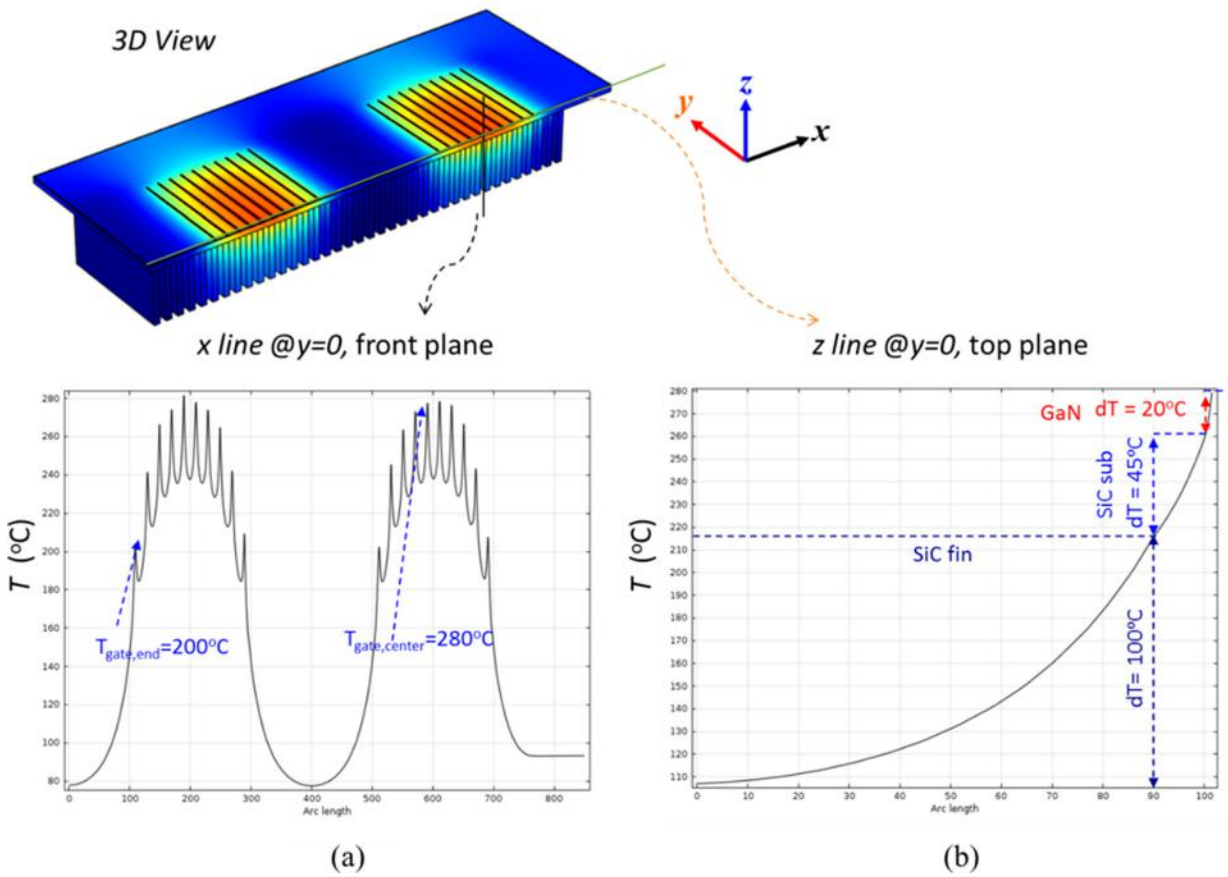

Fig. 6 (*a*) Temperature profile along the *x*-direction at the top surface. (*b*) Temperature rise along the *z*-direction below the hotspot. Note that the dominant temperature rise is from SiC fins.

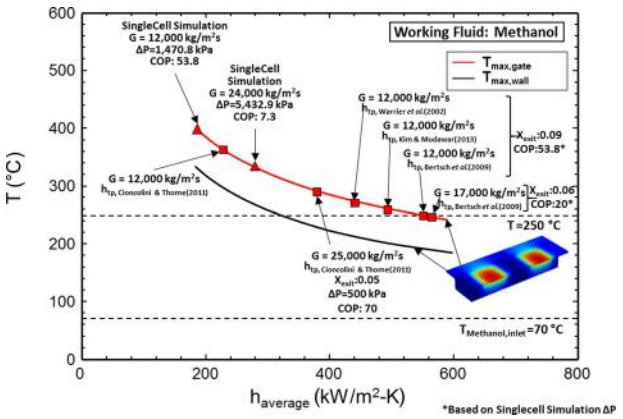

Fig. 7 Junction temperature at gates and the maximum wall temperature below gates with varying convective heat transfer coefficients

segments of the microcooler. Single-phase CFD simulations provide a lower bound for the heat transfer coefficient and pressure drop. CFD simulations are also performed for a single microchannel using a Lee model [22] to provide flow regimes and local temperature fields, which are important to utilize available two-phase boiling heat transfer correlations.

4.1 Computational Domain and Governing Equations for Single-Phase Conjugate CFD Model. A single microchannel from the present microcooler design is used for the computational domain with symmetry boundary conditions applied at the front, back, and inlet side walls as shown in Fig. 8. Methanol flows through the single-cell from the bottom right inlet. After the fluid flows through the 127 μm inlet delivery line, it is introduced to the microchannel and exits through bottom left delivery line. Three different inlet designs are tested to investigate the effect of the pressure drop and heat transfer coefficient as illustrated in Figs. 8(*a*) and 8(*b*). ANSYS FLUENT is used to compute the conservation equations of the single-cell simulation. The constitutive equations are expressed below [23]:

$$\text{Continuity:} \quad \frac{\partial}{\partial t}(\rho) + \nabla \cdot (\rho \mathbf{V}) = 0 \tag{5a}$$

Momentum:

$$\frac{\partial}{\partial t}(\rho \mathbf{V}) + \nabla \cdot (\rho \mathbf{V}\mathbf{V}) = -\nabla P + \nabla \cdot \left[\mu(\nabla \mathbf{V} + \nabla \mathbf{V}^{\mathrm{T}})\right] + \rho \mathbf{g} + \mathbf{F} \tag{5b}$$

$$\text{Energy:} \quad \frac{\partial}{\partial t}(\rho E) + \nabla \cdot (\mathbf{V}(\rho E + P)) = \nabla \cdot (k \nabla T) + Q \tag{5c}$$

Hexahedral mesh is used for the fluid domain and a combination of hexahedral and tetrahedral meshes is applied for the solid domain of different inlet geometries as shown in Fig. 8(*c*). Approximately, a total of 1×10^6 cells are used for the nontapered and for two 45 deg tapered designs. A mesh sensitivity analysis is performed in the microchannel domain. Figure 9 is a plot of the average heat transfer coefficient and wall temperature as a function of mesh size. Both the average heat transfer coefficient and wall temperature reach asymptotic values below a cell (mesh) volume of 3.3 μm^3 for mass fluxes up to 12,000 kg/m^2 s. A finer mesh

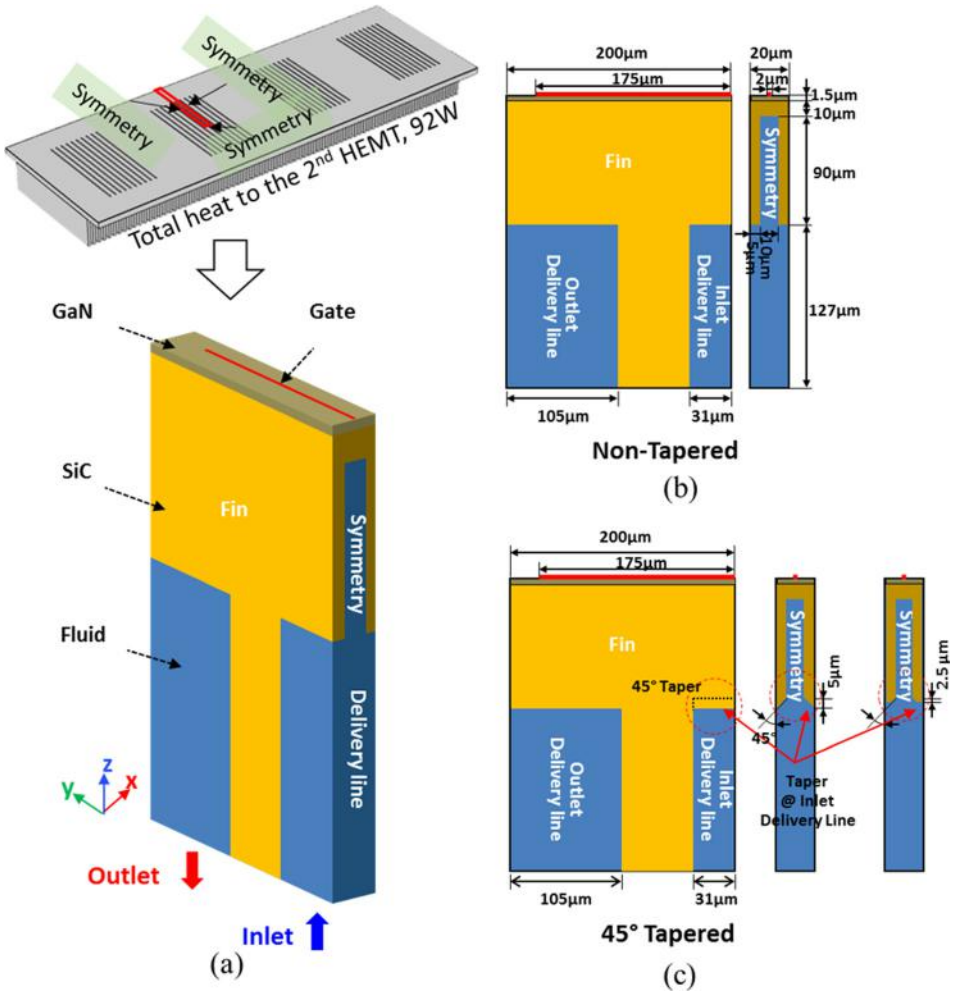

Fig. 8 (*a*) Construction of single-cell computational model, (*b*) front and side view for nontapered model, and (*c*) front and side view for two different 45 deg tapered models

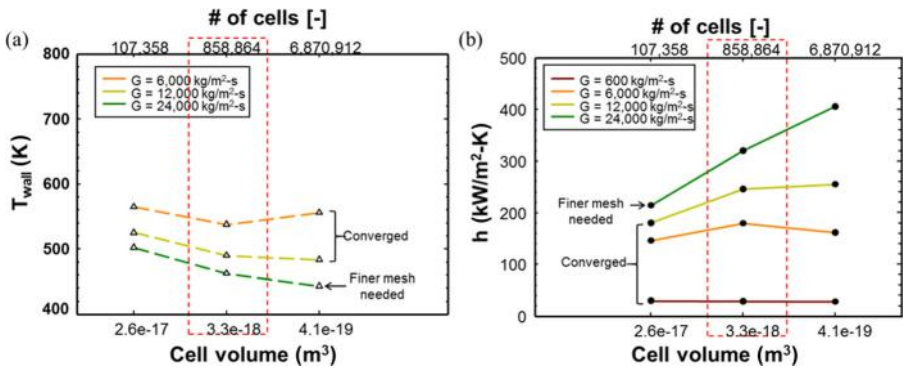

Fig. 9 Average wall temperature and heat transfer coefficient for different mesh sizes

is required for mass fluxes higher than $G = 12{,}000\,\mathrm{kg/m^2\,s}$. In the single-phase simulation, the cell sizes of 1 μm are adopted in the fluid domain to minimize computational efforts.

A pressure-based solver is used for the single-phase single-cell simulation. Turbulent effects are considered using the standard two-equation k–ε turbulent model as prescribed in the ANSYS guide [23], and the semi-implicit method for pressure-linked equations (SIMPLE) [24] is used to tackle pressure–velocity coupling. The PREssure STaggering Option (PRESTO) [24] and the third-order monotonic upstream-centered scheme (MUSCL) for conservation laws [25] are used for pressure and momentum discretization, respectively. The first-order upwind scheme is adopted [24] for both turbulent kinetic energy and specific dissipation rate, and the second-order upwind scheme [24] is used for energy discretization.

4.2 Single-Phase CFD Simulation Results and Discussion. Figures 10(*a*)–10(*c*) show the computed heat transfer coefficients at the microchannel walls for three different mass fluxes of $G = 6000$, 12,000, and $24{,}000\,\mathrm{kg/m^2\,s}$, respectively. The heat transfer coefficient is higher along the inlet of the microchannel,

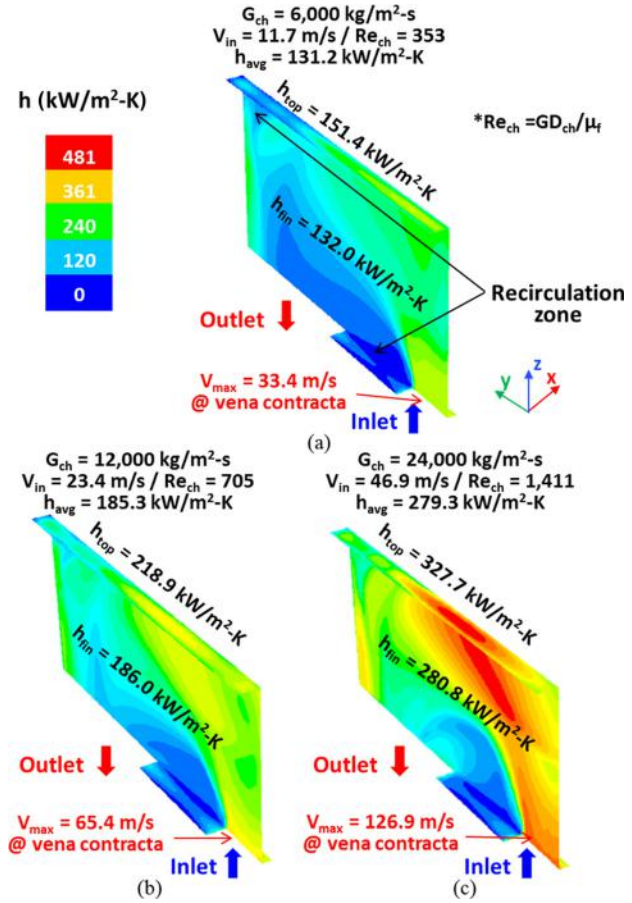

Fig. 10 Computed heat transfer coefficient contour plots for three different mass fluxes of (*a*) $G = 6000\,kg/m^2$ s, (*b*) $G = 12{,}000\,kg/m^2$ s, and (*c*) $G = 24{,}000\,kg/m^2$ s

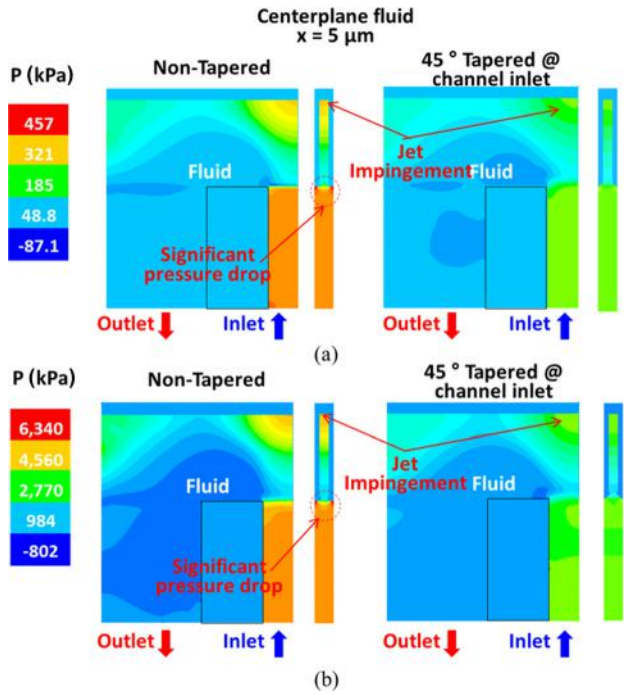

Fig. 11 Computed pressure contour plots of nontapered and 45 deg tapered designs for two different mass fluxes of (*a*) $G = 6000\,kg/m^2$ s and (*b*) $G = 24{,}000\,kg/m^2$ s

where the local velocity field is highest due to the sudden contraction at the entrance. The heat transfer coefficient is relatively higher at the top channel wall compared to the other wall domains due to the impingement effect and is more pronounced as G increases.

Figures 11(*a*) and 11(*b*) show the computed pressure drop results for two different mass fluxes of $G = 6000$ and $24{,}000\,kg/m^2$ s. It should be noted that almost 50% of the total pressure drop occurs at the entrance of the microchannel due to the sudden contraction. Therefore, the 45 deg tapered design shown in Fig. 8(*c*) is a design proposed to minimize the entrance effect. The total pressure drops for the tapered design are significantly reduced compared to those of the nontapered design with negligible changes to the heat transfer coefficient as shown in Fig. 12.

Figure 13 illustrates the computed temperature contour plots at the microchannel side wall, the center of the microchannel, and the top surface of the GaN substrate. The maximum hotspot temperature located at the center of the gate varies from 461 °C for $G = 6000\,kg/m^2$ s to 333 °C for $G = 24{,}000\,kg/m^2$ s, and the corresponding maximum wall temperature at the microchannel also decreases from 387 °C to 259 °C. Figure 14 depicts velocity contours at the centerline of the microchannel and the symmetry inlet side plane for the no-tapered design. The maximum velocity always occurs at the vena contracta of the channel entrance, and it varies from 33.4 m/s to 126.9 m/s. The single-cell simulation results are summarized in Tables 2 and 3.

4.3 Computational Domain and Governing Equations for Two-Phase Boiling Simulation. The single-phase single-cell simulations show that temperatures at the microchannel wall are higher than the saturated temperature, and localized incipient of

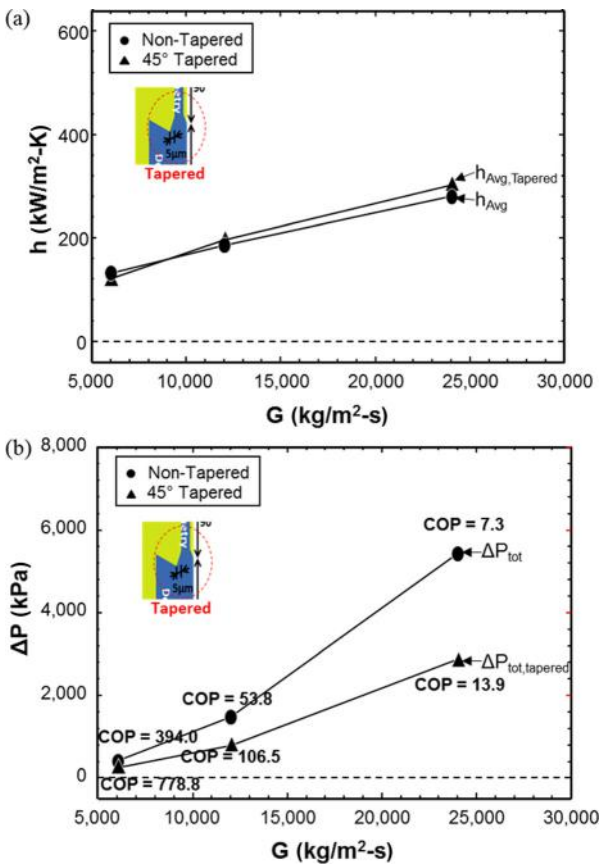

Fig. 12 (*a*) Average heat transfer coefficient and (*b*) pressure drop of three different mass fluxes of $G = 6000$, 12,000, and $24{,}000\,kg/m^2$ s for two different inlet designs

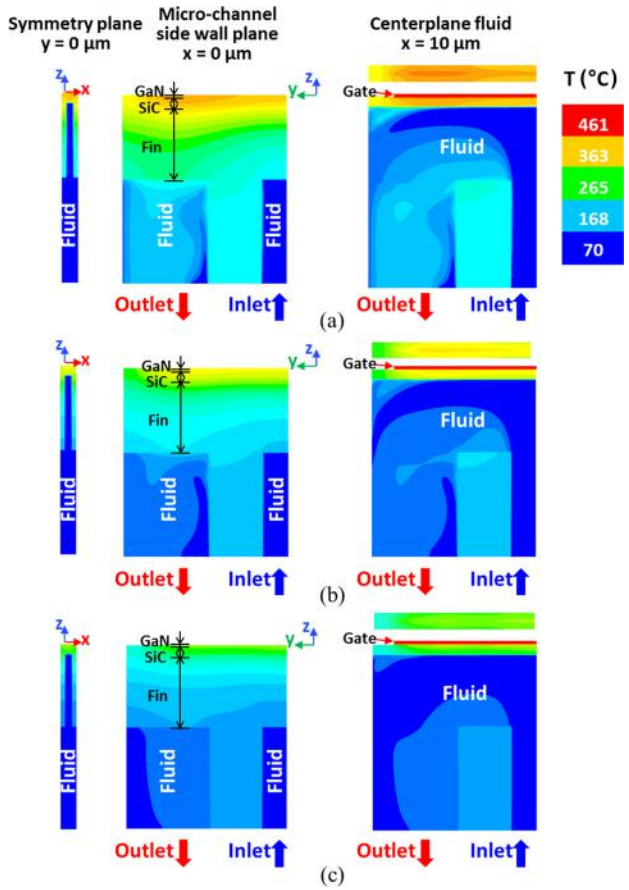

Fig. 13 Computed temperature contour plots for three different mass fluxes of (*a*) $G = 6000\ \text{kg/m}^2\ \text{s}$, (*b*) $G = 12{,}000\ \text{kg/m}^2\ \text{s}$, and (*c*) $G = 24{,}000\ \text{kg/m}^2\ \text{s}$

Table 3 Pressure drops through the single-cell for three different inlet tapered designs

	ΔP (kPa)		
G (kg/m^2 s)	Nontapered	45 deg tapered 1	45 deg tapered 2
6000	402	203	250
12,000	1471	743	848
24,000	5433	2845	3987

boiling may occur at the heated walls. Therefore, a two-phase boiling simulation is performed to investigate flow features under the extreme operating conditions.

The volume of fluid (VOF) method [26] adopted in FLUENT is used to compute the conservation equations for liquid and vapor while also accounting for mass transfer between phases using the Lee model [22], which is expressed as the following equations:

$$S_g = -S_f = r_i\,\alpha_g\,\rho_g\frac{(T - T_{\text{sat}})}{T_{\text{sat}}} \quad \text{for condensation } (T < T_{\text{sat}}) \tag{6}$$

and

$$S_g = -S_f = r_i\,\alpha_f\,\rho_f\frac{(T - T_{\text{sat}})}{T_{\text{sat}}} \quad \text{for evaporation } (T > T_{\text{sat}}) \tag{6b}$$

The continuity equations are expressed as [27]

$$\text{Liquid phase:}\quad \frac{\partial}{\partial t}(\alpha_f\,\rho_f) + \nabla\cdot\left(\alpha_f\,\rho_f\mathbf{V}_f\right) = S_f \tag{7a}$$

$$\text{Vapor phase:}\quad \frac{\partial}{\partial t}(\alpha_g\,\rho_g) + \nabla\cdot\left(\alpha_g\,\rho_g\mathbf{V}_g\right) = S_g \tag{7b}$$

The momentum and energy equations, which are written for the combined phases, are expressed, respectively, as [27]

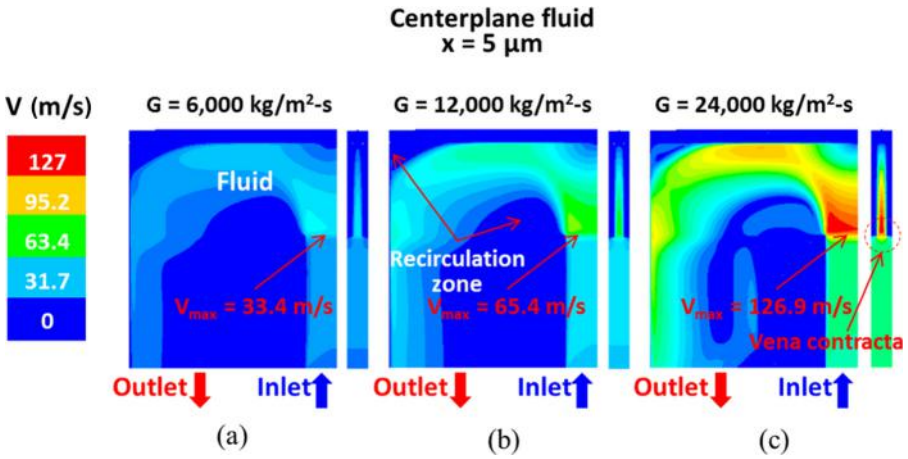

Fig. 14 Computed velocity contour plots for three different mass fluxes of (*a*) $G = 6000\ \text{kg/m}^2\ \text{s}$, (*b*) $G = 12{,}000\ \text{kg/m}^2\ \text{s}$, and (*c*) $G = 24{,}000\ \text{kg/m}^2\ \text{s}$

Table 2 Single-cell simulation results

G (kg/m^2 s)	h_{avg}	$T_{\text{max at gate}}$	$T_{\text{avg at gate}}$	$T_{\text{max at TopGaN}}$	$T_{\text{avg at TopGaN}}$	$T_{\text{max at TopCh}}$	$T_{\text{avg at TopCh}}$	V_{max}	ΔP_{total}	$\Delta P_{\text{total Tapered}}$	$\text{COP}_{\text{Non-Tapered}}$	$\text{COP}_{\text{Tapered}}$
6000	131.3	461	448	423	383	387	368	33.4	402	203	394	789
12,000	185.3	398	390	364	324	323	306	65.4	1471	743	53.8	107
24,000	279.3	333	324	302	261	259	242	127	5433	2845	7.3	13.9

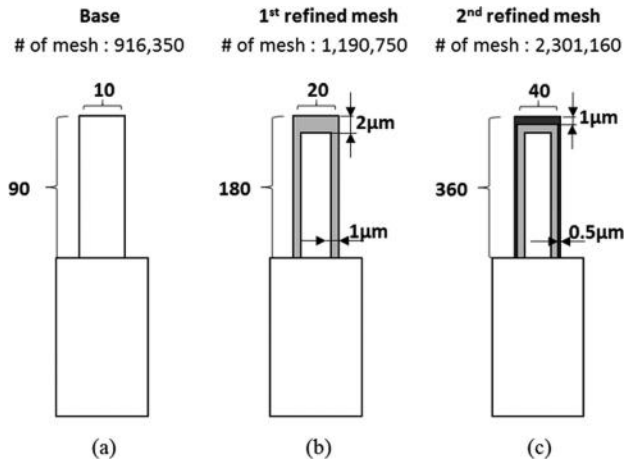

Fig. 15 Three different meshes for VOF single-cell simulation

Momentum:

$$\frac{\partial}{\partial t}(\rho \mathbf{V}) + \nabla \cdot (\rho \mathbf{V}\mathbf{V}) = -\nabla P + \nabla \cdot \left[\mu(\nabla \mathbf{V} + \nabla \mathbf{V}^{\mathrm{T}})\right] + \rho \mathbf{g} + \mathbf{F} \tag{8}$$

Energy:

$$\frac{\partial}{\partial t}(\rho E) + \nabla \cdot (\mathbf{V}(\rho E + P)) = \nabla \cdot (k_{\mathrm{eff}} \nabla T) + Q \tag{9}$$

where E (J/kg) is the energy per unit mass, which is determined from [27]

$$E = \frac{\alpha_f \rho_f E_f + \alpha_g \rho_g E_g}{\alpha_f \rho_f + \alpha_g \rho_g} \tag{10}$$

$$\rho = \alpha_f \rho_f + \alpha_g \rho_g \tag{11a}$$

$$\mu = \alpha_f \mu_f + \alpha_g \mu_g \tag{11b}$$

and

$$k_{\mathrm{eff}} = \alpha_f k_f + \alpha_g k_g \tag{11c}$$

In the present study, mass transfer due to boiling is accounted for using the appropriate mass source terms, S_{f} and S_{g}, which can be obtained from Eqs. 6(*a*) and 6(*b*), and the corresponding energy transfer term can be determined from

$$Q = h_{fg} S_f \tag{12}$$

Both the mass source terms and the energy transfer term are employed into FLUENT using user-defined function macros separately.

The hexahedral meshes with cell sizes of $\Delta c = 1\ \mu\mathrm{m}^3$ are used for the two-phase VOF single-cell simulation. Two additional local refined meshes near the microchannel walls are also tested to check the mesh dependency (Fig. 15) and also to investigate the effect of cell sizes for the interfacial temperature and the mass transfer intensity factor, r_i. The mass flux of $G = 12{,}000\ \mathrm{kg/m^2\ s}$ is

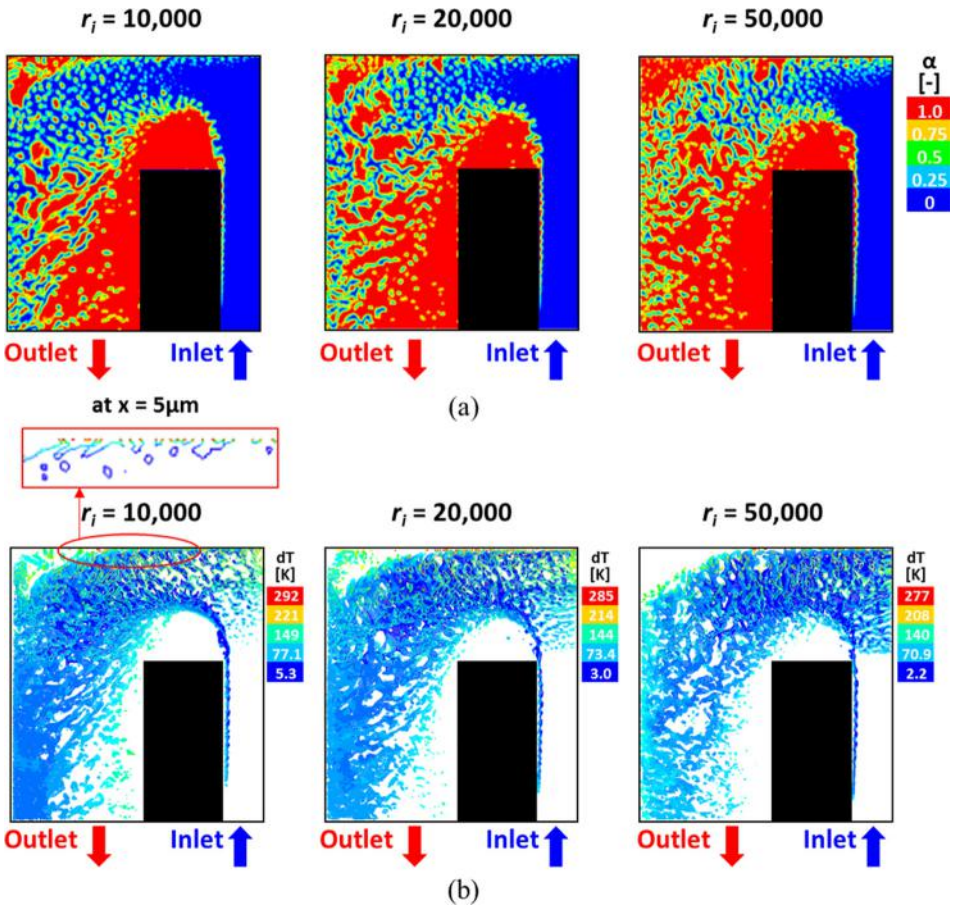

Fig. 16 (*a*) Vapor volume fraction at the centerplane of microchannel and (*b*) temperature difference between the local temperature and the saturated temperature at the interface for three different r_i values of 10,000, 20,000, and 50,000

used for the VOF simulation, and three different r_i values are examined in pursuit of good agreement between the interfacial temperature and the saturated temperature. The variable time-stepping method with a global Courant number of 2 is used to improve convergence for the transient solution

$$\mathrm{Co} = \frac{\mathbf{V}\Delta t}{\Delta c} \tag{13}$$

where $\mathbf{V}$ is the local velocity vector, and Δt and Δc are the time step and cell size, respectively.

The thermodynamic properties shown in Table 1 are used for the two-phase VOF simulation, and the same discretization methods for the single-phase single-cell simulation are used for pressure, momentum, turbulent kinetic energy, specific dissipation rate, and energy. The piecewise linear interface calculation (PLIC) algorithm (named Geo-Reconstruct in FLUENT) [28] is adopted for volume fraction discretization.

A two-step solution procedure is used for the boundary condition at the hotspot area to avoid initial overheating before reaching a quasi-steady state two-phase flow solution [29]. First, a constant temperature boundary condition is applied as the wall boundary condition at the gate, which is estimated from the solid simulation results for a range of heat transfer coefficients. Once the solution reaches a quasi-steady state using the constant temperature boundary condition, it is switched to the constant heat flux boundary condition while monitoring temperature changes at the gate and microchannel walls.

4.4 Two-Phase VOF Simulation Results and Discussion. Figure 16(*a*) shows the vapor volume fractions at the centerplane ($x = 5\ \mu$m) for the three different mass transfer intensity factors of $r_i = 10{,}000$, 20,000, and 50,000 s^{-1}. As illustrated in Fig. 16(*a*), r_i is not only the relaxation constant but also determines how much mass is transferred due to boiling. Therefore, determining an appropriate value for the mass transfer intensity factor, r_i, is one of the most important tasks when using the Lee model [22] for phase change simulations, since it will effect both numerical convergence and flow solutions of the entire two-phase flow field. Researchers have used a very wide range of r_i values, and it increases as computational mesh size decreases due to the developments in central processing unit (CPU) speed. A r_i value of $0.1\ \mathrm{s}^{-1}$ was used in very early phase change studies and relatively much higher values of r_i up to $1.0 \times 10^7\ \mathrm{s}^{-1}$ were used in the recent literature [30]. Since the experimental data are not available for the current microcooler design, the temperature differences, dT, between the local temperature and the saturated temperature at the interface are examined for the three different r_i values to find the appropriate r_i value, which gives the minimum dT at the interface.

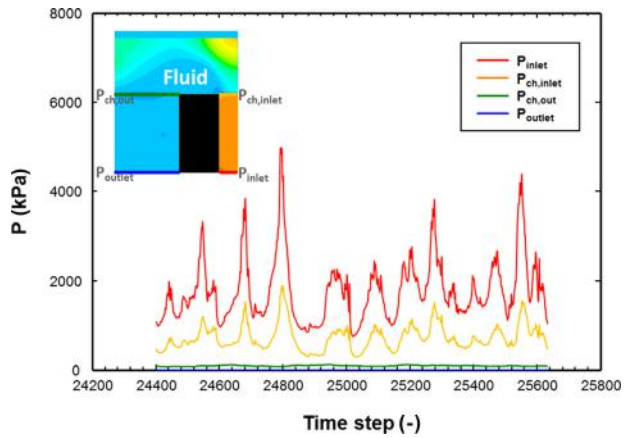

Fig. 17 Local pressure transient at four different locations

Figure 16(*b*) compares the dT at the interface for three different values of $r_i = 10{,}000$, 20,000, and 50,000. The dT shows a wide range of $dT = 2.2$–292 K in the entire fluid domain; however, it should be noticed that the large dT values are only found near the walls and very low dT values such as lower than around 5 K are in the remaining locations. The positive temperature difference along the entire fluid domain indicates that there is insufficient evaporation occurring especially near the heated wall since the r_i value is relatively low to produce enough phase change. As r_i increases, the temperature difference is weakened along the entire fluid domain due to the increase of evaporative cooling, and the minimum dT values are also decreased from 5.3 K to 2.2 K. These results show that r_i should be allowed to vary throughout the entire computational domain to obtain a more accurate solution, which is highly recommended for future study [31–36].

The total pressure drop through the single-cell shows large fluctuation with respect to the time step as shown in Fig. 17, which illustrates the transient local pressure changes at four different locations in the single-cell when $r_i = 50{,}000$. Almost 50% of the entire pressure drop occurs at the entrance of the microchannel as observed in the single-phase simulation results. This large pressure drop at the entrance of the microchannel might work as a flow resistor by inhibiting parallel flow instabilities and consequently keep the system stable, which is a huge advantage for the present microcooler design. Figures 18(*a*) and 18(*b*) show the local centerline temperature at the top of the microchannel wall for $r_\mathrm{i} = 10{,}000$ using the second refined mesh during last 3–4000 iteration time steps. The temperatures continuously increase at the upstream region where $y < 130\ \mu$m and $y > 180\ \mu$m; however, this increase is weakened at the downstream and the temperatures reach the converged values at $150\ \mu\mathrm{m} < y < 180\ \mu\mathrm{m}$.

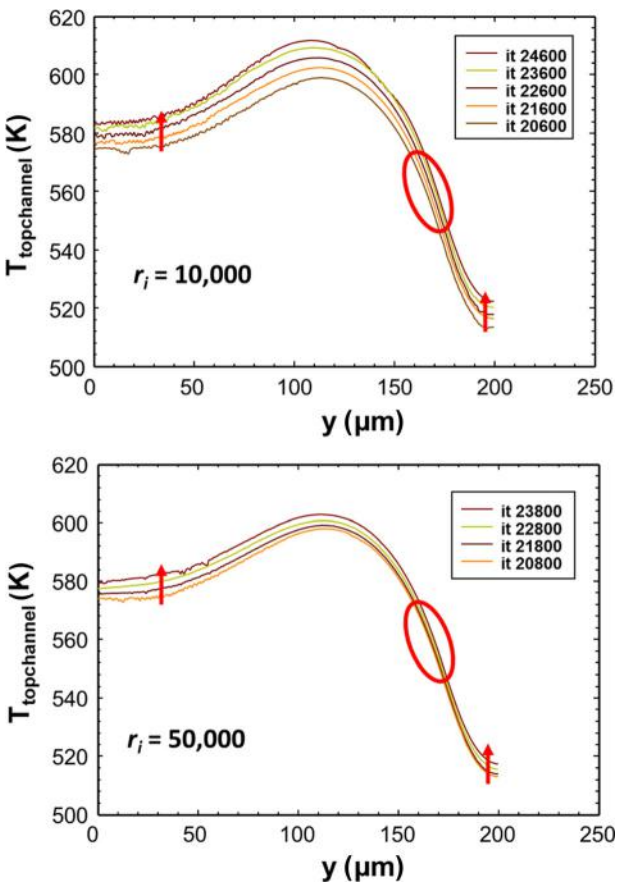

Fig. 18 Transient temperatures at the centerline of top microchannel wall for (*a*) $r_i = 10{,}000$ and (*b*) $r_i = 50{,}000$ using the second finer mesh

The temperature increase is likely due to local dryout and a corresponding low heat transfer coefficient. However, further studies are required to make a conclusion since the heat transfer coefficient and pressure drop vary a relatively large amount depending on different mesh sizes and r_i values in present flow boiling VOF simulations. Therefore, temperature changes for different r_i values associated with different mesh sizes should be carefully investigated in the future.

5 Conclusions

This study explores the advanced cooling solution for extreme heat flux GaN-on-SiC semiconductor devices. The 3D solid conduction simulation and conjugate CFD simulation models have been performed to predict the microcooler performances for the extreme heat flux GaN HEMT applications. The solid conduction simulation models using COMSOL MULTIPHYSICS account for the overall thermal resistances from GaN HEMT to the microchannel walls. The conjugate CFD simulation models using ANSYS FLUENT reveal valuable details on thermofluidic characteristic for both single-phase and two-phase flow of a single-cell configuration. Key findings from the study are as follows:

(1) Conduction simulation models evaluate the thermal performance of the suggested microcooler design with a broad range of heat transfer coefficients by providing temperature distribution.
(2) Single-phase CFD simulations are conducted to obtain the lower bound of total pressure drop and heat transfer coefficient at the microchannel walls for the mass velocity range of $G = 6000$–$24{,}000\,\mathrm{kg/m^2\,s}$.
(3) Single-phase CFD simulations report the local temperature and velocity distributions by identifying the approximate locations of the maximum velocity and recirculation regions that are susceptible to dryouts.
(4) Two-phase CFD simulations are developed using the VOF method by implementing the Lee model. Vapor volume fraction, local temperature, total pressure drop, and heat transfer coefficient results are computed for $G = 12{,}000\,\mathrm{kg/m^2\,s}$ using three different values of $r_i = 10{,}000$–$50{,}000$.

In particular, future studies should conduct experimental validation for the VOF simulation results and calibrate r_i values to improve heat transfer coefficient predictions. r_i values tested in the study can be updated based on the experimental data instead of checking local temperature difference at the interface.

Acknowledgment

This material was based upon work supported by the United States Air Force and DARPA under Contract No. FA-8650-13-C-7374. Any opinions, findings and conclusions or recommendations expressed in this material are those of the author(s) and do not necessarily reflect the views of the United States Air Force and DARPA.

Nomenclature

Bo = boiling number
Co = confinement number, Courant number
D_h = hydraulic diameter
E = energy per unit mass
F = force
g = gravitational acceleration
G = mass velocity
h = heat transfer coefficient
h_{fg} = latent heat
k = thermal conductivity
P = pressure
Q = energy, energy transfer term
q'' = heat flux
r_i = mass transfer intensity factor
Re = Reynolds number
S = mass source term
t = time
T = temperature
V = velocity
w = channel width
We* = modified Weber number
x = quality, coordinate
X_{tt} = Lockhart–Martinelli parameter
y,z = coordinate

Greek Symbols

α = void fraction
μ = dynamic viscosity
ρ = density
σ = surface tension
ϕ = two-phase pressure drop multiplier

Subscripts

AF = annular flow regime
CB = coalescing bubble regime
eff = effective
exit = exit
ext = external
f = liquid
g = vapor
in = inlet
sat = saturated

References

[1] Bar-Cohen, A., John, D. A., and Joseph, J. M., 2011, "Near-Junction Thermal Management for Wide Bandgap Devices," IEEE Compound Semiconductor Integrated Circuit Symposium (CSICS), Waikoloa, HI, Oct. 16–19.
[2] Pengelly, R. S., Simon, M. W., James, W. M., Scott, T. S., and William, L. P., 2012, "A Review of GaN on SiC High Electron-Mobility Power Transistors and MMICs," IEEE Trans. Microwave Theory Tech., **60**(6), pp. 1764–1783.
[3] Bar-Cohen, A., and Peng, W., 2012, "Thermal Management of On-Chip Hot Spot," ASME J. Heat Transfer, **134**(5), p. 051017.
[4] Won, Y., Cho, J., Agonafer, D., Asheghi, M., and Goodson, K. E., 2013, "Cooling Limits for GaN HEMT Technology," IEEE Compound Semiconductor Integrated Circuit Symposium (CSICS), Monterey, CA, Oct. 13–16.
[5] Slack, G. A., 1964, "Thermal Conductivity of Pure and Impure Silicon, Silicon Carbide, and Diamond," J. Appl. Phys., **35**(12), pp. 3460–3466.
[6] Liu, T., Houshmand, F., Gorle, C., Scholl, S., Lee, H., Won, Y., Asheghi, M., Goodson, K. E., Kazemi, H., and Vanhille, K., 2015, "Full Scale Simulation of an Integrated Monolithic Heat Sink for Thermal Management of a High Power Density GaN-SiC Chip," ASME Paper No. IPACK2015-48592.
[7] Calame, J. P., Myers, R. E., Binari, S. C., Wood, F. N., and Garven, M., 2007, "Experimental Investigation of Microchannel Coolers for the High Heat Flux Thermal Management of GaN-on-SiC Semiconductor Devices," Int. J. Heat Mass Transfer, **50**(23), pp. 4767–4779.
[8] Escher, W., Brunschwiler, T., Michel, B., and Poulikakos, D., 2010, "Experimental Investigation of an Ultrathin Manifold Microchannel Heat Sink for Liquid-Cooled Chips," ASME J. Heat Transfer, **132**(8), p. 081402.
[9] Cetegen, E., 2008, "Force Fed Microchannel High Heat Flux Cooling Utilizing Microgrooved Surfaces," Ph.D. dissertation, University of Maryland, College Park, MD.
[10] Linderman, R., Brunschwiler, T., Smith, B., and Michel, B., 2007, "High-Performance Thermal Interface Technology Overview," 13th International Workshop on Thermal Investigation of ICs and Systems (THERMINIC 2007), Budapest, Hungary, Sept. 17–19, pp. 129–134.
[11] Madhour, Y., Zervas, M. N., Schlottig, G., Brunschwiler, T., Leblebici, Y., Thome, J. R., and Michel, B., 2013, "Integration of Intra Chip Stack Fluidic Cooling Using Thin-Layer Solder Bonding," IEEE International 3D Systems Integration Conference (3DIC), San Francisco, CA, Oct. 2–4.
[12] Everhart, L., Jankowski, N., Geil, B., Bayba, A., Ibitayo, D., and McCluskey, P., 2007, "Manifold Microchannel Cooler for Direct Backside Liquid Cooling of SiC Power Devices," ASME Paper No. ICNMM2007-30190.
[13] Dowling, K. M., Suria, A. J., Won, Y., Shankar, A., Lee, H., Asheghi, M., Goodson, K. E., and Senesky, D. G., 2015, "Inductive Coupled Plasma Etching of High Aspect Ratio Silicon Carbide Microchannels for Localized Cooling," ASME Paper No. IPACK2015-48409.

[14] Lee, H., Park, I., Mudawar, I., and Hasan, M. M., 2014, "Micro-Channel Evaporator for Space Applications—2. Assessment of Predictive Tools," Int. J. Heat Mass Transfer, **77**, pp. 1231–1249.
[15] Costa-Patry, E., and Thome, J. R., 2013, "Flow Pattern-Based Flow Boiling Heat Transfer Model for Microchannels," Int. J. Refrig., **36**(2), pp. 414–420.
[16] Lee, H., Park, I., Mudawar, I., and Hasan, M. M., 2014, "Micro-Channel Evaporator for Space Applications—1. Experimental Pressure Drop and Heat Transfer Results for Different Orientations in Earth Gravity," Int. J. Heat Mass Transfer, **77**, pp. 1213–1230.
[17] Houshmand, F., Lee, H., Asheghi, M., and Goodson, K. E., 2015, "High Heat Flux Subcooled Flow Boiling of Methanol in Microtubes," ASME Paper No. IPACK2015-48734.
[18] Kim, S. M., and Mudawar, I., 2013, "Universal Approach to Predicting Saturated Flow Boiling Heat Transfer in Mini/Micro-Channels—Part II. Two-Phase Heat Transfer Coefficient," Int. J. Heat Mass Transfer, **64**, pp. 1239–1256.
[19] Bertsch, S. S., Eckhard, A. G., and Garimella, S. V., 2009, "A Composite Heat Transfer Correlation for Saturated Flow Boiling in Small Channels," Int. J. Heat Mass Transfer, **52**(7), pp. 2110–2118.
[20] Cioncolini, A., and Thome, J. R., 2011, "Algebraic Turbulence Modeling in Adiabatic and Evaporating Annular Two-Phase Flow," Int. J. Heat Fluid Flow, **32**(4), pp. 805–817.
[21] Warrier, G. R., Dhir, V. K., and Momoda, L. A., 2002, "Heat Transfer and Pressure Drop in Narrow Rectangular Channels," Exp. Therm. Fluid Sci., **26**(1), pp. 53–64.
[22] Lee, W. H., 1980, "A Pressure Iteration Scheme for Two-Phase Flow Modeling," *Multiphase Transport: Fundamentals, Reactor Safety, Applications*, Vol. 1, T. N. Veziroğlu, ed., Hemisphere, Washington, DC, pp. 407–431.
[23] ANSYS, 2009, "ANSYS FLUENT 12.1 in Workbench User's Guide," ANSYS, Inc., Canonsburg, PA.
[24] Patankar, S., 1980, *Numerical Heat Transfer and Fluid Flow*, Hemisphere, New York.
[25] Van Leer, B., 1979, "Towards the Ultimate Conservative Difference Scheme. V. A Second-Order Sequel to Godunov's Method," J. Comput. Phys., **32**(1), pp. 101–136.
[26] Hirt, C. W., and Nichols, B. D., 1981, "Volume of Fluid (VOF) Method for the Dynamics of Free Boundaries," J. Comput. Phys., **39**(1), pp. 201–225.
[27] Kharangate, C. R., Lee, H., and Mudawar, I., 2015, "Computational Modeling of Turbulent Evaporating Falling Films," Int. J. Heat Mass Transfer, **81**, pp. 52–62.
[28] Youngs, D. L., 1982, "Time-Dependent Multi-Material Flow With Large Fluid Distortion," *Numerical Methods in Fluid Dynamics*, K. W. Morton and M. J. Baines, eds., Academic Press, New York, pp. 273–285.
[29] Gorle, C., Lee, H., Houshmand, F., Asheghi, M., Goodson, K. E., and Parida, P. R., 2015, "Validation Study for VOF Simulations of Boiling in a Micro-Channel," ASME Paper No. IPACK2015-48129.
[30] Lee, H., Kharangate, C. R., Mascarenhas, N., Park, I., and Mudawar, I., 2015, "Experimental and Computational Investigation of Vertical Downflow Condensation," Int. J. Heat Mass Transfer, **85**, pp. 865–879.
[31] Agostini, B., and Bontemps, A., 2005, "Vertical Flow Boiling of Refrigerant R134a in Small Channels," Int. J. Heat Fluid Flow, **26**(2), pp. 296–306.
[32] Oh, H. K., and Son, C. H., 2011, "Flow Boiling Heat Transfer and Pressure Drop Characteristics of CO_2 in Horizontal Tube of 4.57-mm Inner Diameter," Appl. Therm. Eng., **31**(2), pp. 163–172.
[33] Ducoulombier, M., Colasson, S., Bonjour, J., and Haberschill, P., 2011, "Carbon Dioxide Flow Boiling in a Single Microchannel—Part II: Heat Transfer," Exp. Therm. Fluid Sci., **35**(4), pp. 597–611.
[34] Gungor, K. E., and Winterton, R. H. S., 1986, "A General Correlation for Flow Boiling in Tubes and Annuli," Int. J. Heat Mass Transfer, **29**(3), pp. 351–358.
[35] Harirchian, T., and Garimella, S. V., 2012, "Flow Regime-Based Modeling of Heat Transfer and Pressure Drop in Microchannel Flow Boiling," Int. J. Heat Mass Transfer, **55**(4), pp. 1246–1260.
[36] Shah, M. M., 1982, "Chart Correlation for Saturated Boiling Heat Transfer: Equations and Further Study," ASHRAE Trans., **88**(1), pp. 185–196.